

Autocorrelation signatures in time-resolved black hole flare images: secondary peaks and convergence structure

Zhenyu Zhang,¹ Yehui Hou,¹ Minyong Guo,^{2,3,*} Yosuke Mizuno,^{4,5,6,7,†} and Bin Chen^{8,1,9,‡}

¹*School of Physics, Peking University, No.5 Yiheyuan Rd, Beijing 100871, P.R. China*

²*School of physics and astronomy, Beijing Normal University, Beijing 100875, P. R. China*

³*Key Laboratory of Multiscale Spin Physics (Ministry of Education), Beijing Normal University, Beijing 100875, China*

⁴*Tsung-Dao Lee Institute, Shanghai Jiao-Tong University, Shanghai, 201210, P. R. China*

⁵*School of Physics & Astronomy, Shanghai Jiao-Tong University, Shanghai, 200240, P. R. China*

⁶*Key Laboratory for Particle Physics, Astrophysics and Cosmology,*

Shanghai Key Laboratory for Particle Physics and Cosmology,

Shanghai Jiao-Tong University, Shanghai, 200240, People's Republic of China

⁷*Institut für Theoretische Physik, Goethe Universität, Max-von-Laue-Str. 1, 60438 Frankfurt am Main, Germany*

⁸*Institute of Fundamental Physics and Quantum Technology,*

& School of Physical Science and Technology, Ningbo University, Ningbo, Zhejiang 315211, China

⁹*Center for High Energy Physics, Peking University, No.5 Yiheyuan Rd, Beijing 100871, P. R. China*

The strong gravitational field of a black hole bends light, forming multi-level images, yet extracting precise spacetime information from them remains challenging. In this study, we investigate how gravitational lensing leaves unique and detectable signatures in black hole movies using autocorrelation analysis. By examining the two-dimensional autocorrelation of a movie depicting a hotspot orbiting a Kerr black hole, as viewed by a near-axis observer, we identify a persistent secondary peak structure induced by gravitational lensing. Notably, these secondary peaks converge to a fixed point in the time-angle lag domain, largely independent of the hotspot's orbital radius. This key property suggests that combining future black hole flare observations with advanced autocorrelation analysis could effectively disentangle lensing effects from orbital dynamics, enabling direct measurement of black hole parameters. Our findings establish autocorrelation as a powerful tool for probing spacetime geometry, offering new insights into gravitational physics through time-resolved black hole images.

Introduction. Black holes are among the most enigmatic objects in astrophysics, offering a unique window into the nature of strong-field gravity. The Event Horizon Telescope (EHT) has provided groundbreaking observational evidence for the existence of supermassive black holes by capturing horizon-scale images of M87* and Sgr A* [1, 2]. These images contain rich information about the black hole astrophysical environments, yet extracting the underlying spacetime geometry remains a formidable challenge. To address this, extensive efforts have been dedicated to analyzing photon rings [3], polarization patterns [4, 5], and near-horizon images [6, 7], among others.

A key objective of future EHT observations is the production of time-resolved “black hole movies” [8], which will capture the dynamical evolution of black hole environments with unprecedented detail. Extracting meaningful spacetime information from such time-dependent data necessitates robust analysis techniques. In this context, the two-point correlation function has emerged as a powerful diagnostic tool [9–16]. Strong gravitational lensing produces multiple images of an emission source, giving rise to a primary peak in the autocorrelation function, as well as subpeaks corresponding to cross-correlations between images with different orders [17]. Among these, the secondary peaks—arising from correlations between the zeroth- and first-order images—are particularly significant. However, in the presence of strong intrinsic corre-

lations within accretion flows, these exponentially suppressed secondary peaks are often obscured by the dominant primary maximum. Therefore, the secondary peaks of the autocorrelation have not yet been validated in previous studies based on dynamical accretion flows.

Observations of black hole flares provide a promising avenue for overcoming this limitation. One proposed mechanism for flare production involves the formation of compact, bright regions within the accretion disk near the event horizon. Flares in Sgr A*, observed in X-ray, infrared, and radio bands, are often modeled as compact hotspots [18–28], where emission is dominated by a plasmoid with brightness exceeding the background disk by an order of magnitude [29–33]. Crucially, the intrinsic correlation width of the hotspot scales with its size: smaller, sub-resolution hotspots yield sharper correlation peaks, thereby enhancing the visibility of lensing-induced secondary maxima.

In this letter, we present a rigorous demonstration of autocorrelation analysis as a robust tool for probing spacetime geometry through time-resolved black hole movies. Specifically, we perform numerical simulations of a Kerr black hole observed at low inclination angles, generating images of a compact hotspot on equatorial circular orbits. By computing the two-dimensional autocorrelation of the movie, we successfully isolate the secondary correlation peak and establish its direct correspondence to lensed photon trajectories. A particularly novel result of our analysis is the identification of a fixed point in the peak's position, which is nearly independent of the orbital radius of the hotspot. Our theoretical framework, incorporating analytic modeling, reproduces this universal feature and confirms that it arises from funda-

* Contact author: minyongguo@bnu.edu.cn

† Contact author: mizuno@sjtu.edu.cn

‡ Contact author: chenbin1@nbu.edu.cn

mental spacetime symmetries rather than source-specific dynamics. These findings collectively establish that flare-state movies, when analyzed using autocorrelation techniques, provide a powerful methodology for disentangling gravitational lensing signatures from astrophysical background noise, ultimately enabling direct reconstruction of the black hole spacetime metric. We use the units $G = c = 1$ throughout, so time and length are measured in terms of the black hole mass M .

Autocorrelation of black hole movies. In the context of black hole imaging, the two-point correlation function of the black hole movie is defined as a six-dimensional quantity: $C_{6D} \equiv \langle I(t, \rho, \varphi) I(t', \rho', \varphi') \rangle$, where $I(t, \rho, \varphi)$ denotes the intensity at time t and polar coordinates (ρ, φ) on the observer's screen, and the brackets $\langle \cdot \rangle$ indicate an ensemble average. When the system is statistically stationary and axisymmetric, the time-averaged image becomes independent of t and φ , and the correlation depends only on the time lag $T = t' - t$ and angular separation $\Phi = \varphi' - \varphi$. This symmetry holds exactly for a face-on observer in Kerr spacetime and approximately at low inclinations. Under these conditions, the six-dimensional correlation reduces to a two-dimensional function:

$$C_{2D}(T, \Phi) = \int \rho d\rho \int \rho' d\rho' \langle \Delta I(t, \rho, \varphi) \Delta I(t+T, \rho', \varphi + \Phi) \rangle, \quad (1)$$

where $\Delta I(t, \rho, \varphi) = I(t, \rho, \varphi) - \langle I(t, \rho, \varphi) \rangle$ is the light intensity fluctuation, and the ensemble average can be replaced by time and angular averages:

$$\langle \cdot \rangle = \lim_{\tau \rightarrow \infty} \frac{1}{2\pi\tau} \int_0^\tau dt \int_0^{2\pi} d\varphi. \quad (2)$$

By definition, the two-dimensional autocorrelation has the reflection symmetry, i.e., $C_{2D}(T, \Phi) = C_{2D}(-T, -\Phi)$. Besides, it reaches its maximum when both the angular and time differences are zero, i.e., $C_{2D, \max}(T, \Phi) = C_{2D}(0, 0)$.

In practical implementation, we need to convert the above integrals into discrete Riemann sums. If the time interval between each frame in the black hole movie is t_0 , and we discretize (t, ρ, φ) into (n_t, n_ρ, n_φ) parts respectively, the discretized autocorrelation can be written as:

$$C_{2D}(T, \Phi) \simeq N \sum_{i=1}^{n_\rho} \sum_{i'=1}^{n_\rho} \sum_{j=1}^{n_\varphi} \sum_{k=1}^{n_t} \frac{i}{n_\rho} \frac{i'}{n_\rho} \frac{1}{n_\varphi} \frac{1}{n_t} \Delta I \left(kt_0, \frac{i}{n_\rho}, \frac{2\pi j}{n_\varphi} \right) \Delta I \left(kt_0 + T, \frac{i'}{n_\rho}, \frac{2\pi j}{n_\varphi} + \Phi \right), \quad (3)$$

where N is an overall factor and we can define the normalized autocorrelation by $C(T, \Phi) \equiv C_{2D}(T, \Phi) / C_{2D}(0, 0)$.

Dynamic imaging of hotspots. To calculate autocorrelation, we first generate dynamic imaging of the hotspot source, producing a movie that captures the flare state. We use the slow light treatment for dynamic imaging, where the source evolves during photon motion. This ensures that time delay effects of the multi-level images are correctly reflected in the autocorrelation signal. We focus on the case that the hotspot undergoes

geodesic circular motion. Its angular velocity satisfies

$$\omega_{\text{hs}} = \frac{M^{1/2}}{r_{\text{hs}}^{3/2} + aM^{3/2}}, \quad (4)$$

where r_{hs} is the radius of the circular motion and a is the dimensionless black hole spin parameter. Such orbiting hotspot possesses a translation symmetry along $\partial_t + \omega_{\text{hs}}\partial_\varphi$, which means the system is invariant under $t \rightarrow t + \Delta t$, $\varphi \rightarrow \varphi + \omega_{\text{hs}}\Delta t$. Additionally, we assume the hotspot's emissivity decays exponentially with distance from its center [21], satisfying $J \propto e^{-\frac{x^2}{2s^2}}$, where x is the spatial distance from the emitting point to the hotspot center. Since x^2 depends on both space and time, J also varies accordingly, describing the dynamically evolving source system. Besides, s is a physical quantity characterizing the hotspot size, and we set $s = 0.3M$ in the numerical imaging scheme.

We can then use the general relativistic ray tracing and radiation transfer (GRRT) technique for imaging (see [34, 35] for details). Here, we assume the hotspot is optically thin, allowing us to compute intensity by integrating the redshifted emissivity along a set of light rays. As a result, the observed intensity depends on both the screen coordinates (ρ, φ) and time t . Once $I(t, \rho, \varphi)$ is obtained, we can numerically compute the autocorrelation using Eqs. (3).

Numerical results. For each parameter set used in the autocorrelation computation, we generated 100 hotspot images at a resolution of 512×512 pixels, sampled at intervals of one-hundredth of the orbital period. The main results, shown in Fig. 1 for a fixed spin $a = 0.94$ (with other spins in App. A), include a representative snapshot (left column) and its corresponding autocorrelation (middle column). For $\theta_0 = 1^\circ$, the autocorrelation shows a straight line through the origin, corresponding to the primary maximum from same-order image correlations. This line satisfies $\Phi = \omega_{\text{hs}}T$, consistent with the pattern speed for nearly face-on observers reported in [10]. In this case, the movie inherits the symmetry $\partial_t + \omega_{\text{hs}}\partial_\varphi$ of the hotspot, implying that the autocorrelation is symmetric under $\partial_T + \omega_{\text{hs}}\partial_\Phi$, as seen from Eq. (1).

Secondary maxima, about an order of magnitude weaker, arise from correlations between 0th- and 1st-order images. These share the same slope as the primary maximum but exhibit nonzero intercepts. To keep Φ within $[-\pi, \pi]$ in Fig. 1, we apply $\Phi \bmod 2\pi$. Due to reflection symmetry, the secondary maxima appear as two distinct branches with opposite intercepts.

Fainter parallel lines, an order of magnitude below the secondary maxima, correspond to tertiary maxima from correlations between 0th- and 2nd-order images. These features arise from gravitational lensing, reflecting the multi-image structure encoded in the black hole movie. In principle, an infinite series of such peaks may exist, tracing correlations among higher-order images, but only the tertiary maxima are visible within the limits of our numerical precision.

The top-right panel of Fig. 1 shows the centerlines of the secondary maxima branch with positive intercepts in the (T, Φ) plane for various r_{hs} . These lines are extracted from regions near the maxima and fitted using weighted least squares,

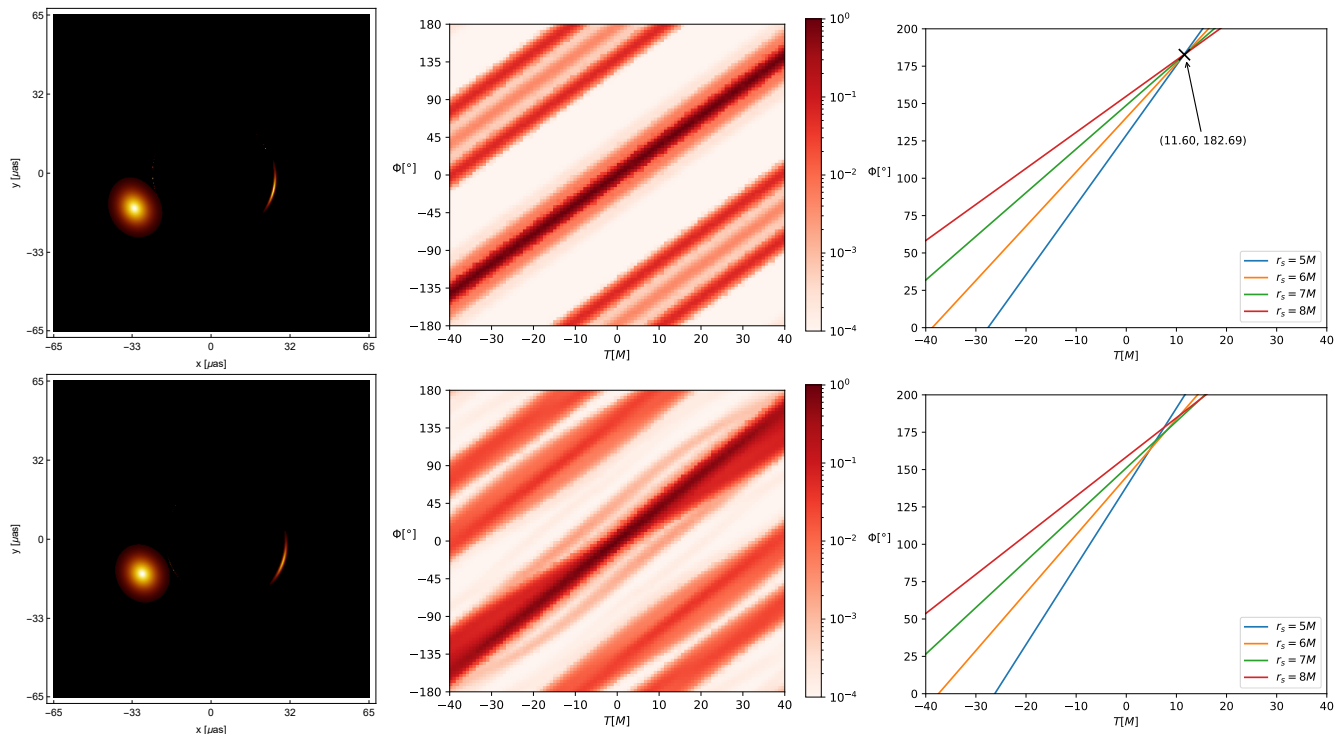


FIG. 1. **Left column:** Snapshots of the hotspot’s image. The black hole spin is set to $a = 0.94$, and the hotspot orbits at a radius of $r_{\text{hs}} = 6M$. The axes are scaled with respect to Sgr A*. **Middle column:** Autocorrelations of the hotspot’s dynamic images, where the color bar represents values on a logarithmic scale. **Right column:** Center lines of the secondary maxima. The fixed point is marked with an “X”. The inclinations are $\theta_o = 1^\circ$ (**Top**) and $\theta_o = 30^\circ$ (**Bottom**), respectively.

with autocorrelation values as weights. For clarity, Φ is shifted to the range $[0, 2\pi]$. Remarkably, all lines intersect at an approximate fixed point: $T = 11.60M$, $\Phi = 182.69^\circ$. This point is obtained by averaging pairwise intersections of four fitted lines. Its existence indicates that, independent of orbital radius, the 0th- and 1st-order images remain correlated at a fixed location. This behavior likely results from the interplay between circular orbital motion and gravitational lensing in Kerr spacetime, as discussed in the next section.

Recent EHT observations suggest a low inclination for Sgr A*, with $\theta_o \lesssim 30^\circ$ [2]. As inclination increases, translational symmetry breaks, yet the hotspot image remains similar to the $\theta_o = 1^\circ$ case (bottom-left panel, Fig. 1). In the bottom-middle panel, secondary maxima remain discernible, though the main peak shape changes and higher-order peaks vanish. To test the persistence of the fixed point at $\theta_o = 30^\circ$, we again fit four secondary-maxima centerlines using weighted least squares (bottom-right panel). While an exact fixed point is no longer evident, the lines still exhibit a clear tendency to converge.

Theoretical explanation. To provide a more explicit analysis of the hotspot’s autocorrelation and the fixed-point effect, we employ a simplified model to study the hotspot’s image. Since our primary focus is on the imprint of gravitational lensing on the autocorrelation, we assume that the hotspot is much smaller than the black hole, allowing us to neglect finite-size effects. For a face-on observer, the hotspot’s image exhibits

translational symmetry under $\partial_t + \omega_{\text{hs}}\partial_\varphi$, and the observed intensity can be expressed as

$$I(t, \rho, \varphi) = \sum_{n=0}^{\infty} F_n \delta_D(\varphi - \omega_{\text{hs}}t - \varphi_n) \frac{\delta_D(\rho - \rho_n)}{\rho_n}, \quad (5)$$

where δ_D denotes the Dirac delta function, while F_n and (ρ_n, φ_n) represent the flux and initial coordinates of the n -th order image on the screen, respectively, which remain constant for a face-on observer. Studies on strong gravitational lensing indicate that, as the order of the images increases, the area of the image undergoes exponential suppression. Consequently, the flux ratio between the images of adjacent orders approximately follows $F_{n+1}/F_n \simeq \exp(-\tilde{\gamma}_0)$, where $\tilde{\gamma}_0$ is the Lyapunov exponent [3]. Since we are primarily interested in the secondary maxima, we retain only the contributions from the 0th and 1st order images in Eq. (5), yielding

$$I^{(01)}(t, \rho, \varphi) \simeq F_0 \delta_D(\varphi - \omega_{\text{hs}}t) \frac{\delta_D(\rho - \rho_0)}{\rho_0} + F_1 \delta_D(\varphi - \omega_{\text{hs}}t - \varphi_1) \frac{\delta_D(\rho - \rho_1)}{\rho_1}. \quad (6)$$

Here, we set $\varphi_0 = 0$, which corresponds to the initial condition where the 0th image passes through $\varphi = 0$ at $t = 0$. Substituting Eq. (6) into the definition (1), we obtain the (un-normalized) autocorrelation:

$$\begin{aligned}
C^{(01)}(T, \Phi) &= \int \rho d\rho \int \rho' d\rho' \left\langle I^{(01)}(t, \rho, \varphi) I^{(01)}(t+T, \rho', \varphi + \Phi) \right\rangle \\
&= \frac{1}{2\pi} \left[(F_0^2 + F_1^2) \delta_D(\Phi - \omega_{\text{hs}}T) + F_0 F_1 \delta_D(\Phi - \omega_{\text{hs}}T - \varphi_1) + F_1 F_0 \delta_D(\Phi - \omega_{\text{hs}}T + \varphi_1) \right].
\end{aligned} \tag{7}$$

The first term in equation (7) represents the primary maximum at $\Phi = \omega_{\text{hs}}T$, where $C^{(01)}(T, \Phi)$ reaches its maximum value, showing excellent agreement with the numerical results in Fig. 1. The second and third terms in equation (7) indicate the presence of secondary maxima at

$$\Phi = \omega_{\text{hs}}T \pm \varphi_1, \tag{8}$$

corresponding to two straight lines in the (T, Φ) plane with a slope of ω_{hs} and intercepts of $\pm\varphi_1$. Since $F_1/F_0 \simeq \exp(-\tilde{\gamma}_0) \simeq 0.08$, the height of the secondary maxima is an order of magnitude smaller than that of the primary maximum.

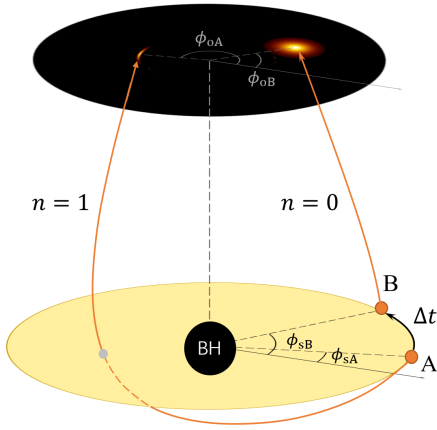


FIG. 2. The imaging process of an orbital hotspot for a face-on observer.

The intercept of the secondary maxima is determined by the angular separation between the 0th- and 1st-order images of the hotspot on the observer's screen at the same moment. Figure 2 illustrates this for a face-on observer: as the hotspot moves from point A to B over a time Δt , light emitted from A (at $\phi = \phi_{s,A}$) completes a half-orbit around the black hole ($n = 1$), reaching the observer with $\phi = \phi_{o,A}$ after time t_A . Meanwhile, light emitted from B (at $\phi = \phi_{s,B}$) travels directly ($n = 0$), arriving at $\phi = \phi_{o,B}$ after time t_B . These two rays arrive simultaneously, forming the 1st- and 0th-order images, respectively. Because the $n = 1$ photon takes longer to reach the observer, the 0th-order image appears at a more advanced angular position, resulting in the observed offset $\varphi_1 = \phi_{o,A} - \phi_{o,B}$. Consequently, we have

$$\Delta t = t_A - t_B = \frac{\phi_{s,A} - \phi_{s,B}}{\omega_{\text{hs}}}. \tag{9}$$

By employing the gravitational lensing formula in Kerr spacetime [36], we can use geodesic integrals to describe the variations in both time and angular position as light propagates

from the hotspot to the observer:

$$\begin{aligned}
\phi_{o,A} &= \phi_{s,A} + I_\phi^{(1)}(r_{\text{hs}}) + \pi, \\
\phi_{o,B} &= \phi_{s,B} + I_\phi^{(0)}(r_{\text{hs}}), \\
t_A &= I_t^{(1)}(r_{\text{hs}}) + a^2 G_t^{(1)}(r_{\text{hs}}), \\
t_B &= I_t^{(0)}(r_{\text{hs}}) + a^2 G_t^{(0)}(r_{\text{hs}}).
\end{aligned} \tag{10}$$

Here, I_t , I_ϕ , G_t and G_ϕ are geodesic integrals and take the forms of elliptic functions [37, 38]. The superscripts indicate the order of the corresponding images. For the face-on observer, the geodesic integrals can be reduced to functions of r_{hs} only. The details can be found in the App. B. By combining equations (9), (10), the intercept φ_1 of the secondary maxima can be written as

$$\begin{aligned}
\varphi_1 &= I_\phi^{(0)}(r_{\text{hs}}) - I_\phi^{(1)}(r_{\text{hs}}) + \omega_{\text{hs}} \left[I_t^{(0)}(r_{\text{hs}}) - I_t^{(1)}(r_{\text{hs}}) \right] \\
&\quad + \omega_{\text{hs}} a^2 \left[G_t^{(0)}(r_{\text{hs}}) - G_t^{(1)}(r_{\text{hs}}) \right].
\end{aligned} \tag{11}$$

Using equations (8) and (11), we can directly compute the secondary maxima for different black hole spins and hotspot orbital radii. We have confirmed that the results are consistent with those presented in Fig. 1.

In particular, we have identified an approximate fixed point associated with the secondary maxima, showing excellent agreement with numerical results. This fixed point, denoted as (T_f, Φ_f) , suggests a robust observational signature: irrespective of the value of r_{hs} , whenever a 0th-order image appears in a black hole movie, a 1st-order image consistently emerges near an angular displacement of Φ_f after a time delay T_f . Crucially, while higher-order images owe their self-similar structure to strong gravitational lensing alone, this fixed point arises from a nontrivial interplay between the hotspot's orbital motion and lensing effects. For a discussion of the impact of higher-order images, see App. C.

Although the fixed point is not exact, we treat it as such in the following analytical derivation, yielding an approximate expression that demonstrates remarkable accuracy and practical utility. The fixed point (T_f, Φ_f) is expected to satisfy

$$\Phi_f = \omega_{\text{hs}}T_f \pm \varphi_1, \quad 0 = (\partial_{r_{\text{hs}}}\omega_{\text{hs}})T_f \pm \partial_{r_{\text{hs}}}\varphi_1, \tag{12}$$

where the second equation follows from the fixed point's insensitivity to variations in r_{hs} . Accordingly, (T_f, Φ_f) is determined by

$$T_f = \mp \frac{\partial_{r_{\text{hs}}}\varphi_1}{\partial_{r_{\text{hs}}}\omega_{\text{hs}}}, \quad \Phi_f = \pm \varphi_1 \left(1 - \frac{\partial_{r_{\text{hs}}}\ln \varphi_1}{\partial_{r_{\text{hs}}}\ln \omega_{\text{hs}}} \right). \tag{13}$$

Note that equation (13) retains a dependence on r_{hs} , indicating that (T_f, Φ_f) represents an approximate—rather than exact—fixed point. For $a = 0.94$ and r_{hs} in the range $5M$ to $8M$,

we find $(T_f, \Phi_f) = (11.47M \pm 0.86M, 181.67^\circ \pm 2.95^\circ)$, demonstrating only a weak dependence on the orbital radius. Consequently, equation (13) provides a novel diagnostic for constraining the black hole spin parameter, as detailed in App. D. Indeed, if the temporal resolution of future EHT observations is finer than $1.72M$ (~ 35 s for Sgr A* and ~ 16 h for M87*), variations in T_f due to changes in r_{hs} will be observationally indistinguishable.

Discussion. By analyzing a simplified hotspot model orbiting a Kerr black hole, we have demonstrated that gravitational lensing leaves distinct imprints on the autocorrelation of black hole movies. Numerical simulations of near-axis observations reveal a persistent secondary peak structure in the two-dimensional autocorrelation. Through theoretical modeling, we conclusively attribute this structure to lensed photon trajectories.

Intriguingly, these secondary peaks converge to a fixed point in the time-angle domain, exhibiting minimal dependence on the hotspot’s orbital radius and instead being primarily governed by the black hole’s spin and mass. This invariance provides a direct and robust means of inferring spacetime metrics without prior knowledge of the emitting source’s dynamics. Our results establish autocorrelation as a powerful, observer-agnostic tool for disentangling gravitational lensing

effects from complex, time-variable emissions. Applying this method to future EHT movies of black hole flares could resolve degeneracies between emission physics and spacetime geometry, enabling precision tests of general relativity in the strong-field regime. These findings highlight the transformative potential of time-resolved black hole imaging in probing the fundamental nature of gravitational physics.

Future research could focus on extending the autocorrelation method to accommodate arbitrary inclination angles and different types of hotspot motion, enhancing its general applicability. Additionally, one important direction for further investigation involves examining the autocorrelation signal in the context of turbulence-driven emission variability, which could be modeled by using numerical simulations [39–41]. Such studies would provide deeper insights into the impact of turbulent dynamics on autocorrelation analyses and improve the robustness of the method under realistic astrophysical conditions.

Acknowledgments. The work is partly supported by NSFC Grant Nos. 12205013 and 12275004. YM is supported by the National Key R&D Program of China (Grant No. 2023YFE0101200), the National Natural Science Foundation of China (Grant No. 12273022), and the Shanghai Municipality Orientation Program of Basic Research for International Scientists (Grant No. 22JC1410600).

-
- [1] **Event Horizon Telescope** Collaboration, K. Akiyama et al., “First M87 Event Horizon Telescope Results. I. The Shadow of the Supermassive Black Hole,” *Astrophys. J. Lett.* **875** (2019) L1, [arXiv:1906.11238 \[astro-ph.GA\]](#).
- [2] **Event Horizon Telescope** Collaboration, K. Akiyama et al., “First Sagittarius A* Event Horizon Telescope Results. I. The Shadow of the Supermassive Black Hole in the Center of the Milky Way,” *Astrophys. J. Lett.* **930** no. 2, (2022) L12, [arXiv:2311.08680 \[astro-ph.HE\]](#).
- [3] M. D. Johnson et al., “Universal interferometric signatures of a black hole’s photon ring,” *Sci. Adv.* **6** no. 12, (2020) eaaz1310, [arXiv:1907.04329 \[astro-ph.IM\]](#).
- [4] Z. Gelles, E. Himwich, D. C. M. Palumbo, and M. D. Johnson, “Polarized image of equatorial emission in the Kerr geometry,” *Phys. Rev. D* **104** no. 4, (2021) 044060, [arXiv:2105.09440 \[gr-qc\]](#).
- [5] Z. Gelles, A. Chael, and E. Quataert, “Signatures of Black Hole Spin and Plasma Acceleration in Jet Polarimetry,” [arXiv:2410.00954 \[astro-ph.HE\]](#).
- [6] A. Chael, M. D. Johnson, and A. Lupsasca, “Observing the Inner Shadow of a Black Hole: A Direct View of the Event Horizon,” *Astrophys. J.* **918** no. 1, (2021) 6, [arXiv:2106.00683 \[astro-ph.HE\]](#).
- [7] Y. Hou, J. Huang, Y. Mizuno, M. Guo, and B. Chen, “Unique Imprint of Black Hole Spin on the Polarization of Near-Horizon Images,” [arXiv:2409.07248 \[gr-qc\]](#).
- [8] **Event Horizon Telescope** Collaboration, K. Akiyama et al., “Mid-Range Science Objectives for the Event Horizon Telescope,” [arXiv:2410.02986 \[astro-ph.HE\]](#).
- [9] K. Fukumura and D. Kazanas, “Light Echos in Kerr Geometry: A Source of High Frequency QPOs from Random X-ray Bursts,” *Astrophys. J.* **679** (2008) 1413, [arXiv:0712.1084 \[astro-ph\]](#).
- [10] N. S. Conroy, M. Bauböck, V. Dhruv, D. Lee, A. E. Broderick, C.-k. Chan, B. Georgiev, A. V. Joshi, B. Prather, and C. F. Gammie, “Rotation in Event Horizon Telescope Movies,” *Astrophys. J.* **951** no. 1, (2023) 46, [arXiv:2304.03826 \[astro-ph.HE\]](#).
- [11] G. N. Wong, “Black Hole Glimmer Signatures of Mass, Spin, and Inclination,” *Astrophys. J.* **909** no. 2, (2021) 217, [arXiv:2009.06641 \[astro-ph.HE\]](#).
- [12] S. Hadar, S. Harikesh, and D. Chelouche, “Extreme lensing induces spectrottemporal correlations in black-hole signals,” *Phys. Rev. D* **107** no. 12, (2023) 124057, [arXiv:2305.11247 \[gr-qc\]](#).
- [13] Q.-H. Zhu, “Photon ring autocorrelations from gravitational fluctuations around a black hole,” *Phys. Rev. D* **109** no. 6, (2024) 064031, [arXiv:2301.00913 \[gr-qc\]](#).
- [14] A. Cárdenas-Avendaño, C. Gammie, and A. Lupsasca, “Explanation for the Absence of Secondary Peaks in Black Hole Light Curve Autocorrelations,” *Phys. Rev. Lett.* **133** no. 13, (2024) 131402, [arXiv:2406.04176 \[astro-ph.HE\]](#).
- [15] G. N. Wong, L. Medeiros, A. Cárdenas-Avendaño, and J. M. Stone, “Measuring Black Hole Light Echoes with Very Long Baseline Interferometry,” *Astrophys. J. Lett.* **975** no. 2, (2024) L40, [arXiv:2410.10950 \[astro-ph.HE\]](#).
- [16] S. Harikesh, S. Hadar, and D. Chelouche, “Exploring lensing signatures through spectrottemporal correlations: implications for black hole parameter estimation,” [arXiv:2502.12053 \[astro-ph.HE\]](#).
- [17] S. Hadar, M. D. Johnson, A. Lupsasca, and G. N. Wong, “Photon Ring Autocorrelations,” *Phys. Rev. D* **103** no. 10, (2021) 104038, [arXiv:2010.03683 \[gr-qc\]](#).

- [18] A. E. Broderick and A. Loeb, “Imaging bright spots in the accretion flow near the black hole horizon of Sgr A*,” *Mon. Not. Roy. Astron. Soc.* **363** (2005) 353–362, [arXiv:astro-ph/0506433](#).
- [19] L. Meyer, A. Eckart, R. Schoedel, W. J. Duschl, K. Muzic, M. Dovciak, and V. Karas, “Near-infrared polarimetry setting constraints on the orbiting spot model for Sgr A* flares,” *Astron. Astrophys.* **460** (2006) 15, [arXiv:astro-ph/0610104](#).
- [20] S. Trippe, T. Paumard, T. Ott, S. Gillessen, F. Eisenhauer, F. Martins, and R. Genzel, “A polarised infrared flare from Sagittarius A* and the signatures of orbiting plasma hotspots,” *Mon. Not. Roy. Astron. Soc.* **375** (2007) 764–772, [arXiv:astro-ph/0611737](#).
- [21] **GRAVITY** Collaboration, M. Bauböck et al., “Modeling the orbital motion of Sgr A*’s near-infrared flares,” *Astron. Astrophys.* **635** (2020) A143, [arXiv:2002.08374](#) [[astro-ph.HE](#)].
- [22] R. Emami et al., “Tracing Hot Spot Motion in Sagittarius A* Using the Next-Generation Event Horizon Telescope (ngEHT),” *Galaxies* **11** no. 1, (2023) 23, [arXiv:2211.06773](#) [[astro-ph.GA](#)].
- [23] M. Wielgus, M. Moscibrodzka, J. Vos, Z. Gelles, I. Marti-Vidal, J. Farah, N. Marchili, C. Goddi, and H. Messias, “Orbital motion near Sagittarius A* - Constraints from polarimetric ALMA observations,” *Astron. Astrophys.* **665** (2022) L6, [arXiv:2209.09926](#) [[astro-ph.HE](#)].
- [24] J. Vos, M. Moscibrodzka, and M. Wielgus, “Polarimetric signatures of hot spots in black hole accretion flows,” *Astron. Astrophys.* **668** (2022) A185, [arXiv:2209.09931](#) [[astro-ph.HE](#)].
- [25] A. Levis, A. A. Chael, K. L. Bouman, M. Wielgus, and P. P. Srinivasan, “Orbital polarimetric tomography of a flare near the Sagittarius A* supermassive black hole,” *Nature Astron.* **8** no. 6, (2024) 765–773, [arXiv:2310.07687](#) [[astro-ph.HE](#)].
- [26] A. I. Yfantis, M. A. Mościbrodzka, M. Wielgus, J. T. Vos, and A. Jimenez-Rosales, “Fitting the light curves of Sagittarius A* with a hot-spot model - Bayesian modeling of QU loops in the millimeter band,” *Astron. Astrophys.* **685** (2024) A142, [arXiv:2310.07762](#) [[astro-ph.HE](#)].
- [27] B. Chen, Y. Hou, Y. Song, and Z. Zhang, “Polarization Patterns of Non-Circular Hotspots around Kerr Black Holes: A Preliminary Study,” [arXiv:2407.14897](#) [[astro-ph.HE](#)].
- [28] J. Huang, Z. Zhang, M. Guo, and B. Chen, “Images and flares of geodesic hot spots around a Kerr black hole,” *Phys. Rev. D* **109** no. 12, (2024) 124062, [arXiv:2402.16293](#) [[gr-qc](#)].
- [29] F. K. Baganoff et al., “Rapid X-ray flaring from the direction of the supermassive black hole at the galactic centre,” *Nature* **413** (2001) 45–48, [arXiv:astro-ph/0109367](#).
- [30] A. Eckart et al., “The flare activity of sgr*: new coordinated mm to x-ray observations,” *Astron. Astrophys.* **450** (2006) 535, [arXiv:astro-ph/0512440](#).
- [31] R. Genzel, F. Eisenhauer, and S. Gillessen, “The Galactic Center Massive Black Hole and Nuclear Star Cluster,” *Rev. Mod. Phys.* **82** (2010) 3121–3195, [arXiv:1006.0064](#) [[astro-ph.GA](#)].
- [32] **GRAVITY** Collaboration, R. Abuter et al., “Detection of orbital motions near the last stable circular orbit of the massive black hole SgrA,” *Astron. Astrophys.* **618** (2018) L10, [arXiv:1810.12641](#) [[astro-ph.GA](#)].
- [33] **GRAVITY** Collaboration, R. Abuter et al., “Polarimetry and astrometry of NIR flares as event horizon scale, dynamical probes for the mass of Sgr A*,” *Astron. Astrophys.* **677** (2023) L10, [arXiv:2307.11821](#) [[astro-ph.GA](#)].
- [34] Z. Zhang, Y. Hou, M. Guo, and B. Chen, “Imaging thick accretion disks and jets surrounding black holes,” *JCAP* **05** (2024) 032, [arXiv:2401.14794](#) [[astro-ph.HE](#)].
- [35] J. Huang, L. Zheng, M. Guo, and B. Chen, “Coport: a new public code for polarized radiative transfer in a covariant framework,” *JCAP* **11** (2024) 054, [arXiv:2407.10431](#) [[astro-ph.HE](#)].
- [36] B. Carter, “Global structure of the Kerr family of gravitational fields,” *Phys. Rev.* **174** (1968) 1559–1571.
- [37] S. E. Gralla and A. Lupsasca, “Null geodesics of the Kerr exterior,” *Phys. Rev. D* **101** no. 4, (2020) 044032, [arXiv:1910.12881](#) [[gr-qc](#)].
- [38] S. E. Gralla and A. Lupsasca, “Lensing by Kerr Black Holes,” *Phys. Rev. D* **101** no. 4, (2020) 044031, [arXiv:1910.12873](#) [[gr-qc](#)].
- [39] O. Porth, Y. Mizuno, Z. Younsi, and C. M. Fromm, “Flares in the Galactic Centre – I. Orbiting flux tubes in magnetically arrested black hole accretion discs,” *Mon. Not. Roy. Astron. Soc.* **502** no. 2, (2021) 2023–2032, [arXiv:2006.03658](#) [[astro-ph.HE](#)].
- [40] M. Najafi-Ziyazi, J. Davelaar, Y. Mizuno, and O. Porth, “Flares in the Galactic centre – II. Polarization signatures of flares at mm-wavelengths,” *Mon. Not. Roy. Astron. Soc.* **531** no. 4, (2024) 3961–3972, [arXiv:2308.16740](#) [[astro-ph.HE](#)].
- [41] H.-X. Jiang, Y. Mizuno, I. K. Dihingia, A. Nathanail, Z. Younsi, and C. M. Fromm, “Dynamics and emission properties of flux ropes from two-temperature GRMHD simulations with multiple magnetic loops,” *Astron. Astrophys.* **688** (2024) A82, [arXiv:2404.03237](#) [[astro-ph.HE](#)].

Appendix A: Numerical results for different spins and radii

In Fig. 3, we present the numerical results for the autocorrelation function corresponding to different black hole spins and hotspot orbital radii. From left to right, each column represents a black hole spin of $a = 0.2, 0.5, 0.94$, respectively. From top to bottom, each row corresponds to a hotspot orbital radius of $r_s = 5M, 6M, 7M, 8M$, respectively. The observer's inclination angle is fixed at $\theta_o = 1^\circ$.

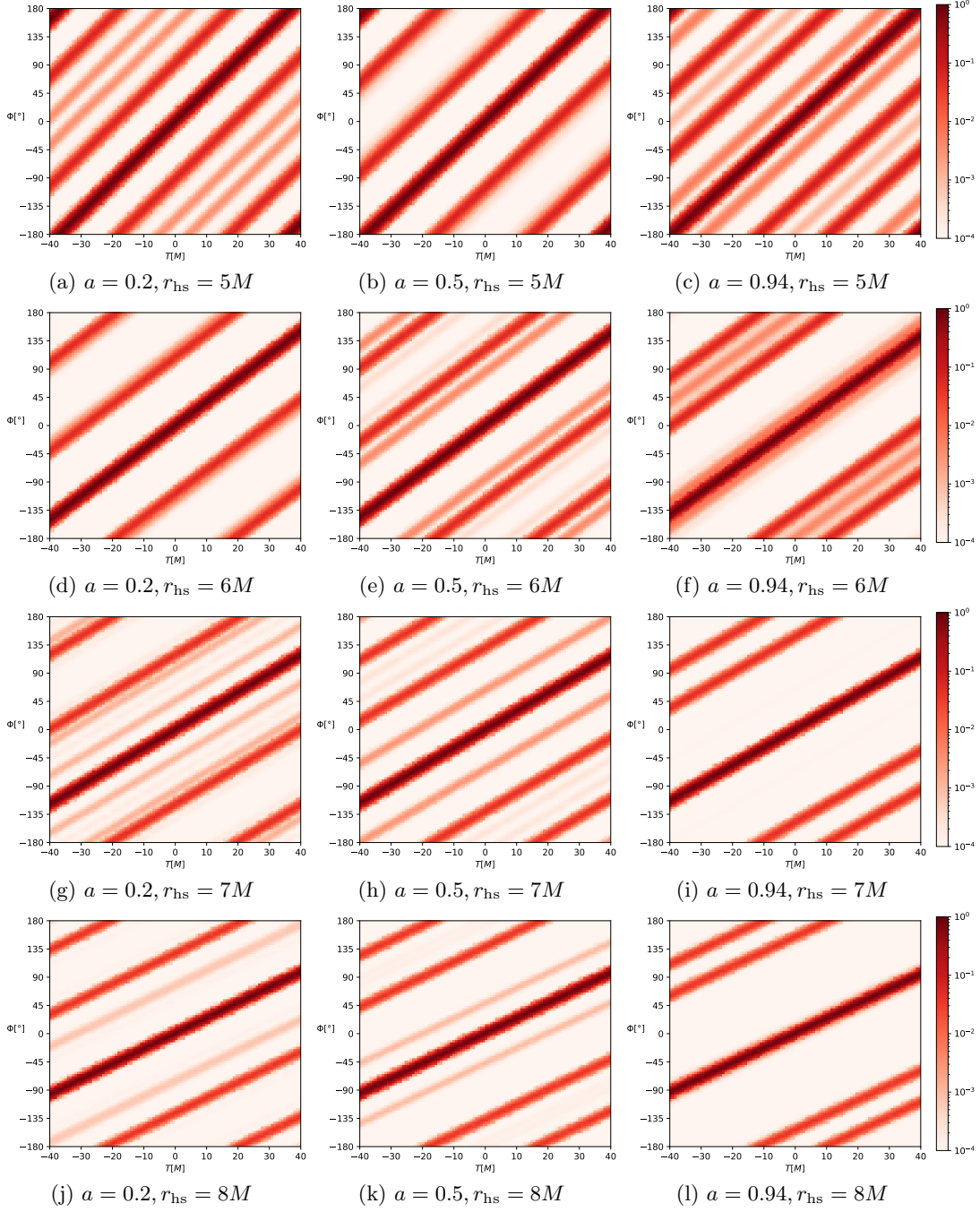


FIG. 3. Autocorrelation for different spins and radii.

For varying spin values, the secondary maximum in the autocorrelation function consistently exhibits an approximate fixed

point; however, its exact position shifts depending on the spin, as illustrated in Fig. 4. In this figure, we again adopt an observer inclination of $\theta_o = 1^\circ$.

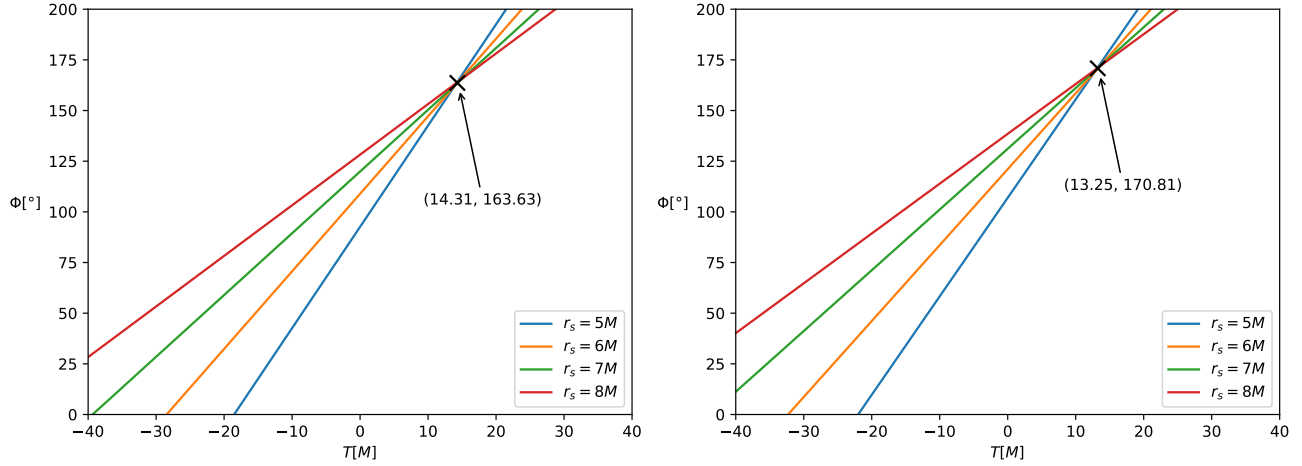


FIG. 4. Secondary maximum fixed points for different black hole spin cases. We fixed $\theta_o = 1^\circ$. The specific coordinate values of this fixed point are obtained by finding the intersection points of four straight lines in pairs and then averaging them. **Left:** $a = 0.2$. **Right:** $a = 0.5$.

Appendix B: Geodesic integrals for photons

In Kerr spacetime, the null geodesic equations governing the propagation of light between the points $(t_s, r_s, \theta_s, \phi_s)$ and $(t_o, r_o, \theta_o, \phi_o)$ are given by the following expressions [36]:

$$\begin{aligned} I_r &= G_\theta, \\ \phi_o - \phi_s &= I_\phi + \lambda G_\phi, \\ t_o - t_s &= I_t + a^2 G_t. \end{aligned} \quad (\text{B1})$$

Here, I_i and G_i are one-dimensional integrals evaluated along the geodesic with respect to r and θ , respectively, and are defined as

$$\begin{aligned} I_r &= \int_{r_s}^{r_o} \frac{dr}{\sqrt{R(r)}}, & G_\theta &= \int_{\theta_s}^{\theta_o} \frac{d\theta}{\sqrt{\Theta(\theta)}}, \\ I_\phi &= \int_{r_s}^{r_o} \frac{a(2Mr - a\lambda)}{\Delta\sqrt{R(r)}} dr, & G_\phi &= \int_{\theta_s}^{\theta_o} \frac{\csc^2 \theta}{\sqrt{\Theta(\theta)}} d\theta, \\ I_t &= \int_{r_s}^{r_o} \frac{r^2 \Delta + 2Mr(r^2 + a^2 - a\lambda)}{\Delta\sqrt{R(r)}} dr, & G_t &= \int_{\theta_s}^{\theta_o} \frac{\cos^2 \theta}{\sqrt{\Theta(\theta)}} d\theta, \end{aligned} \quad (\text{B2})$$

where $\Delta = r^2 - 2Mr + a^2$; λ and η denote the energy-rescaled angular momentum and the rescaled Carter constant, respectively, commonly referred to as the impact parameters; $R(r)$ and $\Theta(\theta)$ represent the effective potentials in the radial and angular directions. Their explicit expressions are given by:

$$\begin{aligned} R(r) &= (r^2 + a^2 - a\lambda)^2 - \Delta [\eta + (\lambda - a)^2], \\ \Theta(\theta) &= \eta + a^2 \cos^2 \theta - \lambda^2 \cot^2 \theta. \end{aligned} \quad (\text{B3})$$

The potential $R(r)$ has four roots, among which only the largest root, denoted as r_t , is relevant for photons escaping to infinity. Consequently, the path integral can be rewritten as

$$\int_{r_s}^{r_o} = \int_{r_s}^{r_t} + 2w \int_{r_t}^{r_s}, \quad (\text{B4})$$

where $w = 0, 1$ represents the number of turning points, indicating the number of times the photon reaches $r = r_t$. Specifically, photons with $w = 0$ correspond to emergent rays, while those with $w = 1$ correspond to reflected rays. The motion in the θ direction exhibits an oscillatory behavior between an upper and a lower bound, denoted as θ_{\pm} . Accordingly, the path integral takes the form of

$$\int_{\theta_s}^{\theta_o} = 2n \int_{\theta_-}^{\theta_+} \pm_s \int_{\theta_s}^{\pi/2} \mp_o \int_{\pi/2}^{\theta_o}, \quad (\text{B5})$$

where $n = 0, 1, 2, \dots$ represents the number of turning points. For photons emitted from an equatorial hotspot and reaching a distant face-on observer, the initial and final angular positions are given by $\theta_s = \pi/2$, $\theta_o = 0$, respectively, with the observer located at $r_o \rightarrow \infty$. In this scenario, the integer n also corresponds to the number of times the photon crosses the equatorial plane. By analyzing the motion in the θ direction, we find that only photons with zero angular momentum, i.e., $\lambda = 0$, can reach the face-on observer. Furthermore, through a simple geometric analysis, the number of turning points in the radial direction satisfies:

$$w = \begin{cases} 1, & r_s > \tilde{r}_0 \text{ and } n > 0, \\ 0, & \text{otherwise,} \end{cases} \quad (\text{B6})$$

where \tilde{r}_0 denotes the radius of the photon sphere relevant to the face-on observer. The first equation in (B1) simplifies to $I_r(r_s, \eta, n) = G_\theta(\eta, n)$, and by solving this equation, we obtain the relationship between the emission radius r_s and the rescaled Carter constant η , labeled as

$$\eta = \eta^{(n)}(r_s). \quad (\text{B7})$$

Due to the geodesic integrals taking the form of elliptic functions and requiring case-by-case analysis, the expression in equation (B7) is highly complex and will not be explicitly presented here. However, for $n = 0$ and sufficiently large r_s , an approximate formula is available [4]:

$$\sqrt{\eta + a^2} \approx \frac{r_s}{M} + 1 + \frac{a^2 - M^2}{2Mr_s} + \frac{50M^2 - 2a^2 - 15M^2\pi}{4r_s^2} + \mathcal{O}(M^3/r_s^3). \quad (\text{B8})$$

Although derived under the limit $r_s \gg M$, the above equation remains a good approximation even at the horizon scale, as demonstrated in Fig. 5 of [38]. Utilizing equation (B7), the geodesic equations for the ϕ and t directions simplify to

$$\begin{aligned} \phi_o - \phi_s &= I_\phi(r_s, \eta^{(n)}(r_s)) + n\pi, \\ t_o - t_s &= I_t(r_s, \eta^{(n)}(r_s)) + a^2 G_t(r_s, \eta^{(n)}(r_s)). \end{aligned} \quad (\text{B9})$$

Clearly, the variations in both time and azimuthal angle depend solely on n and r_s . In this study, we solve equation (B9) numerically. Additionally, for $n = 0$, the change in the azimuthal angle can be approximated by the following piecewise function [27]:

$$\phi_o - \phi_s \approx \begin{cases} \frac{2Ma}{r_s^2} \left[1 - \frac{\tilde{\beta}}{\left(\frac{r_s}{r_H} - 1\right)^{\tilde{\alpha}}} \ln\left(\frac{r_s}{r_H} - 1\right) \right], & r_H < r_s < r_{\text{ms}}, \\ \frac{2Ma}{r_s^2} \left[1 + \frac{\tilde{\gamma}}{\left(\frac{r_s}{r_H} - 1\right)} \right], & r_s \geq r_{\text{ms}}, \end{cases} \quad (\text{B10})$$

where r_H denotes the radius of the event horizon, r_{ms} is the radius of the prograde innermost stable circular orbit (ISCO), and $\tilde{\alpha}, \tilde{\beta}, \tilde{\gamma}$ are three functions of $a_\star = a/M$,

$$\begin{cases} \tilde{\alpha} = 0.035(1 - a_\star) + \frac{0.0059}{(1 - a_\star)^{0.4577}} + 0.1163, \\ \tilde{\beta} = 0.2093 \arctan(a_\star^{12}) + 0.3467, \\ \tilde{\gamma} = 0.07815 \arctan(a_\star^3) + 0.0983. \end{cases} \quad (\text{B11})$$

The function (B10) works well for a large parameter range of a_\star , as is discussed in [27].

Appendix C: Autocorrelation of higher-order images

If we consider the effect of the second-order image, we have:

$$\begin{aligned}
C_{\text{th}}^{(012)}(T, \Phi) &= (F_0^2 + F_1^2 + F_2^2) \delta_D(\Phi - \omega_{\text{hs}}T) \\
&+ F_0 F_1 [\delta_D(\Phi - \omega_{\text{hs}}T - \varphi_1) + \delta_D(\Phi - \omega_{\text{hs}}T + \varphi_1)] \\
&+ F_1 F_2 [\delta_D(\Phi - \omega_{\text{hs}}T + \varphi_2 - \varphi_1) + \delta_D(\Phi - \omega_{\text{hs}}T + \varphi_1 - \varphi_2)] \\
&+ F_0 F_2 [\delta_D(\Phi - \omega_{\text{hs}}T - \varphi_2) + \delta_D(\Phi - \omega_{\text{hs}}T + \varphi_2)].
\end{aligned} \tag{C1}$$

We find that without using the near-photon-ring approximation, the correlations between the first-order and second-order images do not overlap at the same positions as the correlations between the zero-order and first-order images. Below we conduct the near-ring approximation and give a discussion of higher-order images.

For higher-order images, the ratio between successive fluxes satisfies $F_{n+1}/F_n \simeq \exp(-\tilde{\gamma}_0)$, where $\tilde{\gamma}_0$ is the Lyapunov exponent associated with the photon sphere at $r = \tilde{r}_0$. To facilitate calculations, we artificially extend the critical behavior of higher-order images to arbitrary orders. However, the resulting error in the final outcome is predominantly due to the contributions from the 0th and 1st images. Under this approximation, the intensity can be expressed as

$$I(t, \rho, \varphi) \simeq F_0 \sum_{n=0}^{\infty} e^{-n\tilde{\gamma}_0} \delta_D(\varphi - \omega_{\text{hs}}t - \varphi_n) \frac{\delta_D(\rho - \rho_n)}{\rho_n}, \tag{C2}$$

and the (unnormalized) autocorrelation function is given by

$$\begin{aligned}
C(T, \Phi) &= \int \rho d\rho \int \rho' d\rho' \langle I(t, \rho, \varphi) I(t+T, \rho', \varphi + \Phi) \rangle \\
&\simeq F_0^2 \sum_{n,m} e^{-(n+m)\tilde{\gamma}_0} \lim_{\tau \rightarrow \infty} \frac{1}{2\pi\tau} \int_0^\tau dt \int_0^{2\pi} d\varphi \delta_D(\varphi - \omega_{\text{hs}}t + \varphi_n) \delta_D(\varphi + \Phi - \omega_{\text{hs}}(t+T) + \varphi_m) \\
&= \frac{F_0^2}{2\pi} \sum_{n,m} e^{-(n+m)\tilde{\gamma}_0} \delta_D(\varphi_m - \varphi_n + \Phi - \omega_{\text{hs}}T).
\end{aligned} \tag{C3}$$

From the expression of the intensity (C2), we see that φ_n represents the azimuthal angle of the n -th photons on the observer's screen at $t_o = 0$. According to the lensing effect for higher-order images, the relationship between the emission and arrival positions of photons is given by [38]

$$\begin{aligned}
\varphi_n - \phi_s^{(n)} &\simeq \left(n + \frac{1}{2}\right) \tilde{\delta}_0 + D, \\
t_o - t_s^{(n)} &\simeq \left(n + \frac{1}{2}\right) \tilde{\tau}_0 + H,
\end{aligned} \tag{C4}$$

where $\tilde{\delta}_0$ and $\tilde{\tau}_0$ are the critical parameters in t and ϕ directions, respectively, associated with the photon sphere at $r = \tilde{r}_0$. The quantities D and H are functions of the emission radius. Therefore, we can obtain

$$\begin{aligned}
\varphi_n - \varphi_m &\simeq \omega_{\text{hs}}(t_s^{(n)} - t_s^{(m)}) + (n-m)\tilde{\delta}_0 \\
&= \omega_{\text{hs}}(m-n)\tilde{\tau}_0 + (n-m)\tilde{\delta}_0,
\end{aligned} \tag{C5}$$

where we have used the relation $\phi_s^{(n)} - \phi_s^{(m)} = \omega_{\text{hs}}(t_s^{(n)} - t_s^{(m)})$ for an emission source following a circular orbit. By utilizing equation (C5), we can rewrite the autocorrelation function as

$$\begin{aligned}
C(T, \Phi) &\simeq \frac{F_0^2}{2\pi} \sum_{n,m} e^{-(n+m)\tilde{\gamma}_0} \delta_D\left((m-n)(\tilde{\delta}_0 - \omega_{\text{hs}}\tilde{\tau}_0) + \Phi - \omega_{\text{hs}}T\right) \\
&= \frac{F_0^2}{2\pi} \sum_{n=m} e^{-2n\tilde{\gamma}_0} \delta_D(\Phi - \omega_{\text{hs}}T) \\
&+ \frac{F_0^2}{2\pi} \sum_{n>m} e^{-(n+m)\tilde{\gamma}_0} \delta_D\left((m-n)(\tilde{\delta}_0 - \omega_{\text{hs}}\tilde{\tau}_0) + \Phi - \omega_{\text{hs}}T\right) \\
&+ \frac{F_0^2}{2\pi} \sum_{n>m} e^{-(n+m)\tilde{\gamma}_0} \delta_D\left((n-m)(\tilde{\delta}_0 - \omega_{\text{hs}}\tilde{\tau}_0) + \Phi - \omega_{\text{hs}}T\right),
\end{aligned} \tag{C6}$$

and by defining $q = |n - m|$, we finally obtain the following expression:

$$C(T, \Phi) \simeq \frac{1}{2\pi} \frac{F_0^2}{(1 - e^{-2\tilde{\tau}_0})} \sum_{-\infty}^{\infty} e^{-|q|\tilde{\tau}_0} \delta_D \left(\Phi - \omega_{\text{hs}} T - q(\tilde{\delta}_0 - \omega_{\text{hs}}\tilde{\tau}_0) \right). \quad (\text{C7})$$

In the above expression, the term with $q = 0$ corresponds to the primary maximum, arising from the overall superposition of correlations between images of the same order. The peaks suppressed by $\exp(-|q|\tilde{\tau}_0)$ originate from the correlation between images whose order differs by q . In the (T, Φ) plane, the intercepts of these peaks of the autocorrelation function are given by $q(\tilde{\delta}_0 - \omega_{\text{hs}}\tilde{\tau}_0)$, indicating that for correlations between higher-order images, the intercept is jointly determined by the critical parameters and the angular velocity of the hotspot. Given that the critical parameters are approximately $\tilde{\delta}_0 \simeq \pi$, $\tilde{\tau}_0 \simeq 3\sqrt{3}M\pi$ [38], for an angular velocity satisfying $\omega_{\text{hs}} \ll (3\sqrt{3}M)^{-1}$, the peak intercepts are predominantly governed by $\tilde{\delta}_0$. In the case of Keplerian motion, this condition holds when $r_{\text{hs}} \gg 3M$.

Appendix D: Measuring the black hole spin by the fixed point

Figure 5 presents the evolution of the approximate fixed-point as a function of the spin parameter. The left panel illustrates the variation in the time coordinate, while the right panel displays the corresponding change in the angular coordinate. The black curves represent numerical averages of the intersection points of the secondary maxima across different values of r_{hs} . The shaded region, derived from equation (13), corresponds to the theoretical uncertainty estimate, encompassing the range where r_{hs} varies from $5M$ to $8M$. It is evident that T_f decreases monotonically with increasing spin, while ϕ_f increases. As r_{hs} varies from $5M$ to $8M$, T_f changes by approximately $2M$. In contrast, as the spin parameter a increases from 0.01 to 0.99, T_f varies by about $3.5M$. The angular coordinate exhibits even more pronounced variations: as r_{hs} changes within the same range, ϕ_f varies by approximately 8° , whereas increasing a from 0.01 to 0.99 results in a change of about 26° . This suggests that the observed position of ϕ_f could serve as a useful indicator for distinguishing between high-spin and low-spin black holes in future observations.

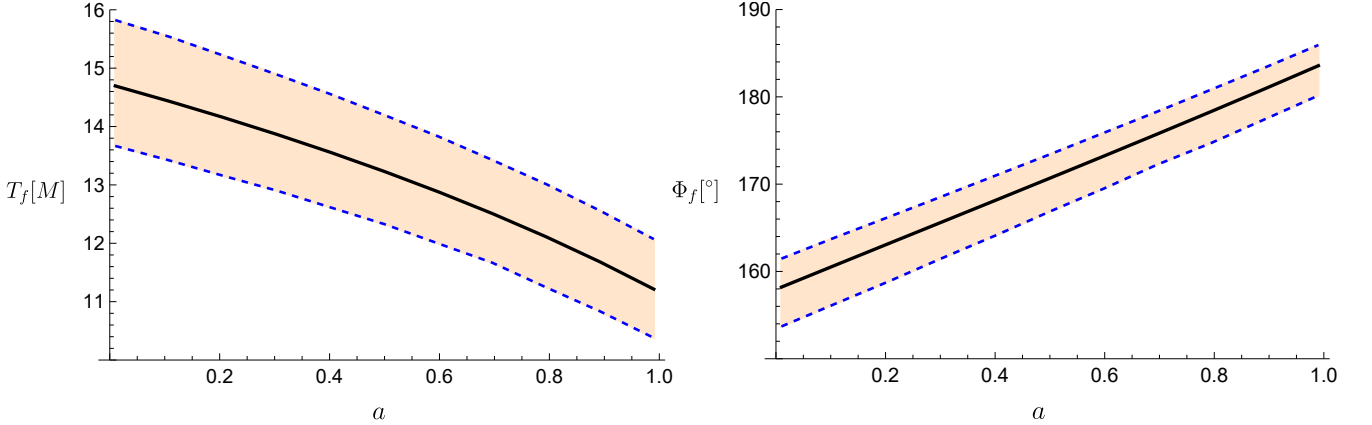


FIG. 5. The spin dependence of the time and angular coordinates of the fixed point.

To further evaluate the efficacy of the fixed point in characterizing black hole parameters, we present a concrete demonstration of how the approximate fixed point can be employed to estimate the black hole spin. As a specific example, consider a hotspot orbiting a black hole with spin parameter $a = 0.7$ at a radius of $r_{\text{hs}} = 8.5M$. By performing a numerical autocorrelation analysis on the simulated movie, we identify the secondary maximum, denoted by the gray dotted line in Fig. 6. Using this hypothetical observational feature as the sole input, we then apply the fixed-point method to estimate the black hole spin.

For the nearly face-on case, the slope of the hypothetical observed line gives the angular velocity of the hotspot, given by equation (4). This allows us to constrain r_{hs} to the range $8.43M$ to $8.66M$, assuming the spin parameter lies between 0 to 1. Within this interval, the trajectory of the theoretically predicted fixed point (given by equation (13)) is represented by the shaded region in Fig. 6. The black hole spin can then be determined from the intersection between the hypothetical observed line and this shaded region, yielding a spin estimate of 0.699-0.700. Although the fixed point shifts slightly with variations in r_{hs} , we find that the resulting uncertainty in the inferred spin remains exceptionally small.

Furthermore, the fixed-point method maintains its reliability even when the estimated range of r_{hs} is substantially relaxed. As demonstrated in Fig. 7, when we extend the orbital radius bounds from the precise interval $[8.43M, 8.66M]$ to a broader range of $[6M, 10M]$, the method still yields a spin estimate between 0.699 and 0.728, which remains remarkably accurate compared to

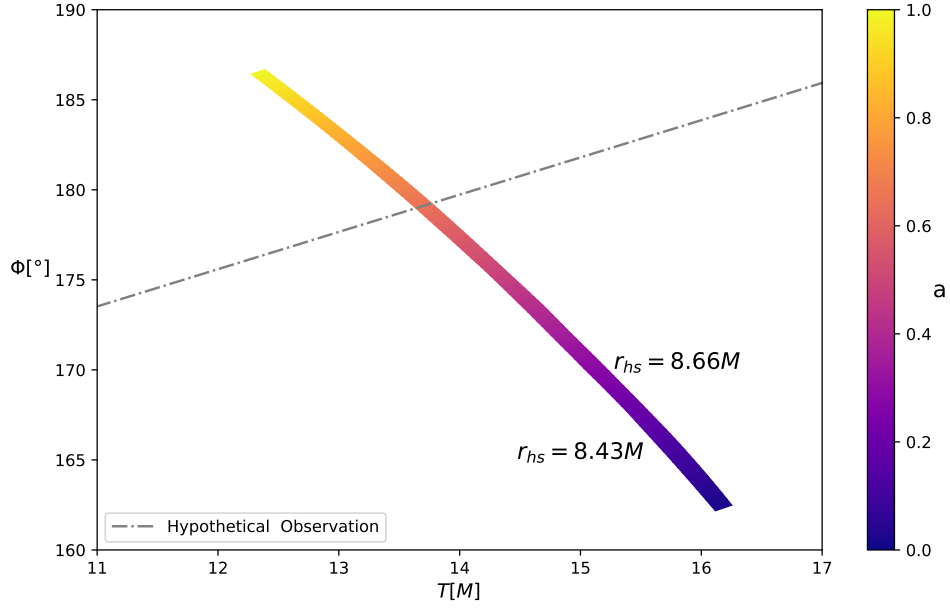


FIG. 6. Fixed point shift as r_{hs} varies from $8.43M$ to $8.66M$ and a from 0 to 1. The gray dotted line represents the secondary maximum of a hypothetical observation with $a = 0.7$ and $r_{\text{hs}} = 8.5M$.

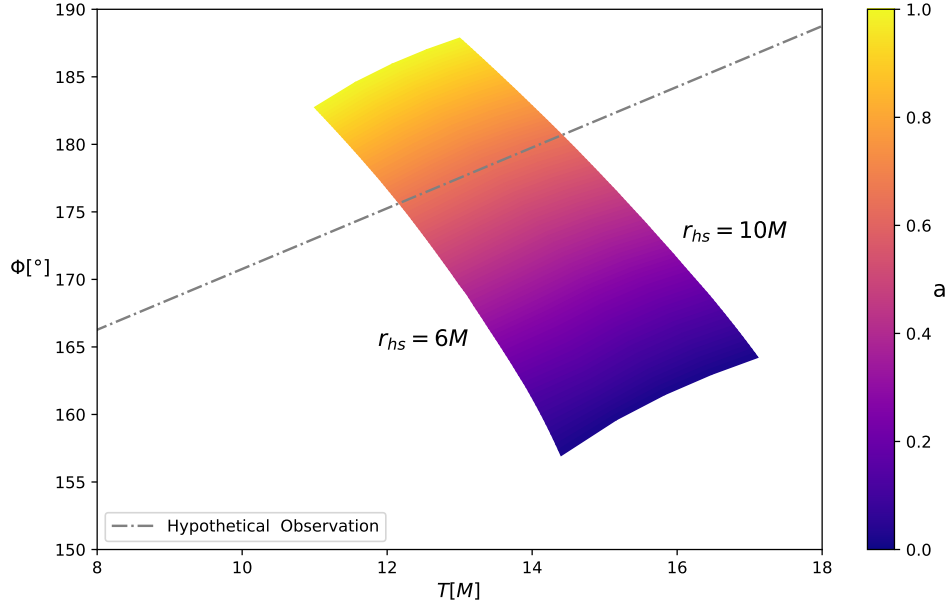


FIG. 7. Fixed point shift as r_{hs} varies from $6M$ to $10M$ and a from 0 to 1. The gray dotted line represents the secondary maximum of a hypothetical observation with $a = 0.7$ and $r_{\text{hs}} = 8.5M$.

other methods. The robustness of this approach stems from two key factors: (1) the consistently positive slope of the hypothetical observed line, and (2) the small acute angle it forms with the equal-spin contours. These geometric characteristics ensure minimal variation in the inferred spin parameter across the overlapping region.